Dynamic stability of centrifugal pendulum vibration absorbers allowing a rotational mobility

Vincent Mahé, Alexandre Renault, Aurelien Grolet, Olivier Thomas, Hervé Mahé

Dynamic stability of centrifugal pendulum vibration absorbers allowing a rotational mobility

V. Mahe [a,b,*], A. Renault [b], A. Grolet [a], O. Thomas [a], H. Mahe [b]

[a] *Arts et Metiers Institute of Technology, LISPEN, HESAM Université, F-59000 Lille, France*
[b] *Valeo Transmissions, Centre d'Étude des Produits Nouveaux, Espace Industriel Nord, Route de Poulainville, 80009 Amiens Cedex 1, France*

A B S T R A C T

Centrifugal pendulum vibration absorbers (CPVA) are used in the automobile industry to reduce the vibrations of the transmission system. These passive devices are made of several masses oscillating along a given trajectory relative to the rotor. In this paper, the dynamic stability of a new class of CPVA is investigated. The particularity of this new class is that masses now admit a significant rotation motion relative to the rotor, in addition to the traditional translation motion. The efficiency of such devices is optimal for a perfect synchronous motion of the oscillating masses. However, masses unison can be broken for the benefit of energy localisation on a given absorber, leading to a loss of mitigation performances. To assess the stability of such devices, a dynamical model based on an analytic perturbation method is established. The aim of this model is to predict analytically localisation and jumps of the response. The validity of the model is confirmed through a comparison with both a numerical resolution of the system's dynamics and an experimental study.

1. Introduction

In the frame of reduction of polluting emissions and fuel consumption of vehicles using thermal engines, automotive manufacturers try to reduce the cylinder capacity and engine speed of rotation. These evolutions lead to a significant increase of rotation irregularities called ‘‘acyclisms", mainly due to higher combustion pressure. One of the main characteristics of these reciprocating engines is the linear dependence of the acyclism frequency to the mean engine speed of rotation. The coefficient of proportionality is called the engine (or firing) order and only depends on the architecture of the engine. For four strokes engines, the engine order is half the number of cylinders. During acceleration phase, the engine sweeps a wide frequency range containing some driveline torsional modes. This situation may lead to significant noise and vibration levels into the passenger compartment and premature wear of the driveline components. Centrifugal pendulum vibration absorbers (CPVA) have been used for many years to minimise acyclisms of automotive powertrains at the engine order. These passive devices consist of oscillating masses (pendulums) moving along particular paths relative to a primary inertia (rotor) as shown in Fig. 1. The operation principle of the CPVA is that of a tuned mass damper whose stiffness is proportional to the mean engine speed. This enables it to remain tuned on the engine order to reduce torsional vibrations of the rotor.

CPVA exhibit strong non-linearities: geometric non-linearities due to the large amplitude of motion, and inertial non-linearities, for instance due to Coriolis effect. The non-linear response of a CPVA is strongly affected by the choice of the pendulums' trajectory. D. E. Newland observed early on that circular trajectories may exhibit unstable periodic responses, leading to jumps of the

* Corresponding author at: Arts et Metiers Institute of Technology, LISPEN, HESAM Université, F-59000 Lille, France.
E-mail addresses: vincent.mahe@ensam.eu (V. Mahe), alexandre.renault@valeo.com (A. Renault), aurelien.grolet@ensam.eu (A. Grolet), olivier.thomas@ensam.eu (O. Thomas), herve.mahe@valeo.com (H. Mahe).

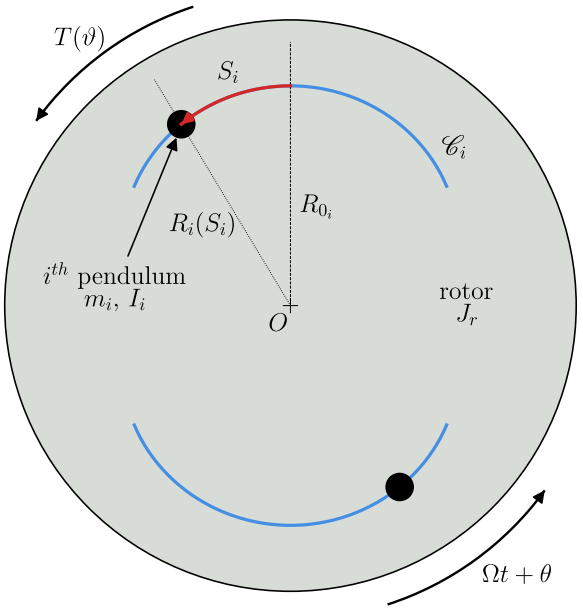

Fig. 1. Representation of the system studied for $N = 2$ pendulums.

response [1]. Since the works of H. H. Denman, the preferred trajectories are epicycloids because they are almost tautochronic [2]. Due to their cyclic symmetry, CPVA are subject to non-linear energy localisation phenomena. Such situations, which might decrease the efficiency of the absorbers, have been studied by S. Shaw et al. [3–7], A. Grolet et al. [8] and K. Nishimura et al. [9] in the case of translated pendulums, i.e. pendulums that do not rotate relatively to the rotor. Until recent times, such pendulums were the only ones used in the industry. However, A. Renault and M. A. Acar showed that adding a rotational mobility of the pendulums may lead to a significant increase of mitigation performances [10–13]. This increase in performance was also observed by J. Mayet and H. Ulbrich [14]. Recent works by M. Cirelli, M. Cera et al. [15–19] confirmed the interest for pendulums with a rotational mobility and introduced a new way a representing the trajectory, using curvature ratios instead of the polynomial coefficients used in most studies (see [4] for instance). M. Cirelli et al. also used a Cartesian representation of the trajectory to derive tuning recommendations consistent with known results of the literature [20]. J. Mayet and H. Ulbrich [21] used Hamilton's formalism to compute the stability of a CPVA with rotating pendulums and gave guidelines regarding the tuning of the system. X. Tan et al. considered a CPVA made of a single pendulum obeying a non-linear rotation law and gave guidelines for the choice of this law [22]. E. R. Gomez et al. investigated theoretically and experimentally the friction losses in a CPVA with rotating pendulums [23]. A new type of CPVA, made of a double pendulum, was studied by V. Manchi and C. Sujatha [24]. The use of CPVA to damp multidegrees-of-freedom systems was considered by K. Kadoi et al. [25]. B. Geist et al. [26] studied the precision requirements and sources of errors associated with the manufacturing process of a bifilar CPVA.

The motivation of this paper is to investigate the stability of CPVA whose pendulums rotate relatively to the rotor. Unlike previous studies [16,18,21], the authors chose to describe the trajectory and rotation functions of a pendulum using polynomials (in [16,18], curvature ratios and a rolling radius are used to describe the trajectory and rotation law, respectively, whilst in [21] the trajectory and rotation are not defined explicitly). This way, the non-linear parts of the trajectory and rotation will appear clearly in the results, allowing for an easier understanding of their impact on the dynamics. To facilitate further this understanding, a tool representing the stability as a function of the trajectory and rotation functions is introduced. New design guidelines are derived from these analysis. Finally, experimental observations of the localised response are used to validate the analytical model. To our knowledge, it is the first time that the analytical prediction of the localisation is compared to experimental results (localisation was observed unexpectedly in [27] and not compared to analytical predictions in [28]).

This paper is organised as follows: Section 2 describes the modelling of the CPVA. Section 3 presents a linear study of the CPVA, setting the basis of the non-linear analysis. This non-linear analysis starts in Section 4 where the simplified pendulums' equation is established. This equation is solved in Section 5 and its stability is assessed. Section 6 presents a case study of the former developments. A numerical validation of the model is shown and an original visualisation of the stability in the design space is introduced. Design rules are proposed in Section 7 and an experimental validation is lead in Section 8. Finally, this paper ends with a conclusion in Section 9.

2. Modelling

The system studied is shown in Fig. 1. It is made of a rotor of inertia J_r rotating about its centre O. Its total angular position is $\vartheta(t) = \Omega t + \theta(t)$ where t is the time, Ω is the mean rotation velocity and θ corresponds to the fluctuating part of the rotation.

A torque $T(\vartheta)$ is applied to this rotor. It can be decomposed into a constant torque T_0 and a periodic one $T_\theta(\vartheta)$. The constant torque balances the torque arising from the rotor's damping, thus setting the mean rotation speed Ω. In the model, an equivalent linear viscous damping b_r is used for the rotor. N pendulums of mass m_i and inertia I_i (about their centre of gravity) oscillate on their trajectory $\mathscr{C}_i$. The position of their centre of gravity on these trajectories is given by the curvilinear abscissa $S_i(t)$ and their distance from the centre of rotation of the rotor is $R_i(S_i)$. The characteristic dimension $R_{0_i} = R_i(S_i = 0)$ represents the position of the pendulums at rest (when $T_\theta = 0$ such that they are perfectly centrifugated). In addition to the traditional translation motion, the present study considers that the pendulums rotate relatively to the rotor according to the rotation function $\alpha_i(S_i)$. As for the rotor, an equivalent linear viscous damping b_i is used to model the damping between the rotor and the i^{th} pendulum. In the later, pendulums and their associated trajectory and rotation functions will be considered identical so that subscript "i" will be dropped when addressing pendulums' parameters. Using the relation between the mean torque, the rotor's damping and the mean rotation speed, $T_0 = b_r\Omega$, and introducing the non-dimensional parameters and variables $s_i = S_i/R_0$, $\eta = I/mR_0^2$, $\bar{b} = b/m\Omega$, $x(s_i) = R(R_0 s_i)^2/R_0^2$, $z(s_i) = \sqrt{x(s_i) - (dx(s_i)/ds_i)^2/4}$, $\gamma(s_i) = R_0 d\alpha(R_0 s_i)/d(R_0 s_i)$, $\mu = NmR_0^2/(J_r + NI)$, $\bar{b}_r = b_r/(J_r + NI)\Omega$, $\bar{T}_0 = T_0/(J_r + NI)\Omega^2$, $\bar{T}_\theta = T_\theta/(J_r + NI)\Omega^2$, $\tau = \Omega t$, the equations of motion can be written as

$$\frac{1}{N}\left[\sum_{i=1}^{N}(N + \mu x(s_i))\theta'' + \mu\left(z(s_i) + \eta\gamma(s_i)\right)s_i'' + \mu s_i'\left(\frac{dx(s_i)}{ds_i}(1+\theta') + \frac{dz(s_i)}{ds_i}s_i' + \eta\frac{d\gamma(s_i)}{ds_i}s_i'\right)\right] + \bar{b}_r\theta' = \bar{T}_\theta(\tau+\theta), \tag{1a}$$

$$\left(z(s_i) + \eta\gamma(s_i)\right)\theta'' + \left(1 + \eta\gamma(s_i)^2\right)s_i'' + \eta\gamma(s_i)\frac{d\gamma(s_i)}{ds_i}s_i'^2 - \frac{1}{2}\frac{dx(s_i)}{ds_i}\left(1+\theta'\right)^2 + \bar{b}s_i' = 0, \quad i = 1, \dots, N \tag{1b}$$

where $(\bullet)'$ denotes derivation with respect to τ. Eq. (1a) is related to the motion of the rotor and the N Eqs. (1b) represent the motion of the pendulums. It is chosen to express the trajectory and rotation functions as polynomials such that

$$x(s_i) = 1 - n_t^2 s_i^2 + \sum_{k=3}^{\infty} x_{[k]}s_i^k, \quad \alpha(s_i) = \sum_{k=0}^{\infty}\alpha_{[k]}s_i^k \tag{2}$$

where n_t is called the trajectory order of the pendulums and $x_{[k]}$, $\alpha_{[k]}$ are trajectory and rotation coefficients. Note that in the case $x_{[k]} = 0\ \forall k$, the pendulums' trajectories are epicycloids, which corresponds to the tautochronic trajectory for $\theta = 0$ [2].

From now on, it is assumed that the fluctuating torque applied to the rotor contains only one harmonic. This is justified by the fact that in reciprocating engines, the fundamental harmonic typically dominates the fluctuating torque. The non-dimensional form of the fundamental torque harmonic is $\bar{T}_1\cos[n(\tau+\theta)]$ where n is the engine order. For a car thermal engine, n corresponds to the number of strikes per revolution of the crankshaft. At this stage, $\bar{T}_1\cos[n(\tau+\theta)]$ is not a periodic forcing term but a non-linear term as it depends on θ. In the following, two methods are proposed to transform it into a periodic forcing term.

Method 1. One can use the change of independent variable $\tau \to \tau + \theta$ proposed by S. Shaw et al. [29] to directly transform $\bar{T}_1\cos[n(\tau+\theta)]$ into a periodic forcing term. This choice is motivated by the fact that the explosions of a car engine do not depend on time but on the angular position of the crankshaft (which is the same as that of the rotor). Though it adds non-linearities to the system, this method is interesting as it does not require any hypothesis, thus keeping the equations exact.

Method 2. Another method is to express the fluctuating torque as a function of τ to write $\bar{T}_1\cos((\omega/\Omega)\tau)$ where ω is the angular frequency of the acyclism. For a car engine, the excitation frequency must correspond to the number of strikes per second, leading to $\omega = n(\Omega + \dot{\theta})$ where $(\dot{\bullet})$ refers to a derivation with respect to time. It can be assumed that the fluctuating rotation velocity of the crankshaft is much smaller than the mean rotation speed, i.e. $\dot{\theta} \ll \Omega$. It follows that $\omega/\Omega \approx n$, leading to a trivial transformation of the torque into a periodic forcing term.

3. Linear vibrations of the system

In this section, a linear analysis of the system is led. After transforming the external torque into a periodic forcing term using *Method 2* (*cf.* Section 2), one can linearise Eqs. (1a) and (1b) and then use a property of arrowhead matrices [30] to find that the eigenorders and eigenvectors of the system are

$$\begin{gathered} n_{00} = 0, \quad n_{10} = n_p, \quad n_{20} = n_p\sqrt{\frac{1+\mu}{1+\mu\left(1-\frac{\Lambda_c^2}{\Lambda_m}\right)}}, \quad \boldsymbol{\phi_{00}} = [1, 0, \dots, 0]^T, \quad \boldsymbol{\phi_{20}} = \left[-\frac{\mu\Lambda_c}{1+\mu}, 1, \dots, 1\right]^T, \\ \boldsymbol{\phi}_{\mathbf{10}_i}[i+1] = -\boldsymbol{\phi}_{\mathbf{10}_i}[i+2] = 1, \ \boldsymbol{\phi}_{\mathbf{10}_i}[j \neq \{i+1, i+2\}] = 0, \quad i = 1, \dots, N-1. \end{gathered} \tag{3}$$

Superscript T denotes the transpose. Λ_m and Λ_c are constants representing the equivalent mass of a pendulum and the linear coupling term between a pendulum and the rotor, respectively. They are given by

$$\Lambda_m = 1 + \eta\alpha_{[1]}^2, \quad \Lambda_c = 1 + \eta\alpha_{[1]} \tag{4}$$

where $\alpha_{[1]}$ is the linear rotation coefficient. n_p is the eigenorder of the pendulums when the rotor is spinning at constant speed. Considering the case $\theta = 0$ and linearising Eqs. (1b), one finds that n_p is related to n_t such that

$$n_p = n_t\Lambda_m^{-1/2}. \tag{5}$$

When a fluctuating torque is applied on the rotor, pendulums generate an antiresonance at order n_p (in the conservative case). Thus, for a fluctuating torque of order n, one must choose $n_p = n$ to minimise the vibrations of the rotor (this can be extended to the non-conservative case as damping is small). For this reason, n_p is called the tuning order of the pendulums. It is interesting to note that if $\alpha_{[1]} \neq 0$, then $\Lambda_m > 1$, leading to $n_t > n_p$ (*cf.* Eqs. (4) and (5)). This means that the relative rotation of the pendulums imposes an over-tuning of the trajectory order compared to the case of purely translated pendulums (for which $n_t = n_p$).

$\boldsymbol{\phi_{00}}$ is a rigid body mode for which only the rotor is excited. $\boldsymbol{\phi_{10_i}}$ are $N-1$ degenerated modes for which pendulums i and $i+1$ are out of phase while other pendulums are immobile ($i = 1, \dots, N-1$). They are associated to the eigenvalue n_{10}, which has a multiplicity $N-1$ and the rotor is a node of these modes. Note that in the case $N = 2$, $\boldsymbol{\phi_{10}}$ is not degenerated and simply corresponds to an out-of-phase motion of the pendulums. $\boldsymbol{\phi_{20}}$ is a mode for which pendulums move in unison but in phase-opposition with respect to the rotor (provided that $\Lambda_c > 0$, which is the case in practice).

This section offers a linear analysis of the CPVA. However, it can be seen from Eqs. (1a) and (1b) that the dynamics of the system is subject to several sources of non-linearity. In the following, an analytical model allowing the visualisation and prediction of non-linear phenomena will be derived.

4. Simplification of the equations

Following S. Shaw et al. [4,7,31], the construction of the model starts with a scaling of the parameters, allowing a simplification of the equations of motion such that the dynamics of the pendulums becomes uncoupled from that of the rotor. Since the displacement of the pendulums will be considered small, the trajectory and rotation functions (2) are truncated so that

$$x(s_i) = 1 - n_t^2 s_i^2 + x_{[4]} s_i^4 + \mathcal{O}(s_i^6), \quad \alpha(s_i) = \alpha_{[1]} s_i + \alpha_{[3]} s_i^3 + \mathcal{O}(s_i^5) \tag{6}$$

will be used in the following computations. There are no odd powers of s_i in $x(s_i)$ and no even powers in $\alpha(s_i)$ so that these two functions are symmetric (anti-symmetric, respectively) about $s_i = 0$. It is the case in practice due to design constraints. The fluctuating rotor's rotation is a priori made of several harmonics such that it can be expanded as

$$\theta = \theta^{(1)} + \theta^{(2)} + HOT \tag{7}$$

where $\theta^{(1)}$ and $\theta^{(2)}$ are the first and second harmonics, respectively, and HOT refers to *Higher Order Terms*.

4.1. Scaling

In this subsection, the aim is to scale the weight of some parameters and variables so as to capture the desired physical phenomena. The following hypothesis and remarks will govern the scaling:

- The optimum system configuration is that with small damping (both rotor's and pendulums' dampings). This way, the vibration amplitude of the rotor at its antiresonance is very small.
- The fluctuating torque T_θ is small compared to the rotor's kinetic energy (which is $J_r \Omega^2/2$ at equilibrium). This implies that $\bar{T}_1$ is small.
- The total pendulums' geometric inertia about point O, NmR_0^2, is considered small compared to the inertia of the total rotating system, $J_r + NI$, such that μ is small.
- The rotor's inertia being significant, the fluctuating rotation speed $\dot{\theta}$ is small compared to the mean rotation speed. Note that this hypothesis was already done in Section 3 to transform the external torque into a periodic excitation.
- The pendulums' amplitude of motion is small compared to their distance from the centre of rotation O such that s_i are small.
- The trajectory function chosen (*cf.* Eq. (6)) is an epicycloid perturbed by $x_{[4]} s_i^4$. Considering the perturbation is small, $x_{[4]}$ is a priori small.
- The rotation function chosen (*cf.* Eq. (6)) differs from a linear rotation by the term $\alpha_{[3]} s_i^3$. Considering rotation is mainly linear, $\alpha_{[3]}$ is a priori small.

Accordingly to the above and introducing the small parameter ϵ, the following scaled parameters are introduced

$$\bar{b} = \epsilon^{\ell} \tilde{b}, \quad \bar{b}_r = \epsilon^{h} \tilde{b}_r, \quad \bar{T}_1 = \epsilon^{r} \tilde{T}_1, \quad \mu = \epsilon^{\phi} \tilde{\mu}, \quad \theta^{(1)} = \epsilon^{w_1} \tilde{\theta}^{(1)}, \quad \theta^{(2)} = \epsilon^{w_2} \tilde{\theta}^{(2)}, \quad s_i = \epsilon^{\nu} \tilde{s}_i, \quad x_{[4]} = \epsilon^{p} \tilde{x}_{[4]}, \quad \alpha_{[3]} = \epsilon^{q} \tilde{\alpha}_{[3]} \tag{8}$$

where ℓ, h, r, ϕ, w_1, w_2, ν, p and q are scaling coefficients to be determined. In order to give a physical meaning to ϵ, one can choose to set $\epsilon = \mu$ [4].

4.2. Rotor's dynamics

The aim here is to obtain an equation governing the rotor's dynamics as a function of the pendulums' and the external torque. Introducing the trajectory and rotation functions (6), the expanded form of θ (7) and the scaled parameters (8) in the rotor's Eq. (1a) and setting $r = \phi + \nu$, one can write

$$\epsilon^{w_1} \tilde{\theta}^{(1)\prime\prime} + \epsilon^{w_2} \tilde{\theta}^{(2)\prime\prime} = \epsilon^{r} \left[\tilde{T}_1 \cos(n\tau) + \frac{n_p^2 \tilde{\mu} \Lambda_c}{N} \sum_{i=1}^{N} \tilde{s}_i \right] + \epsilon^{r+\nu} \frac{2\tilde{\mu} n_t^2}{N} \sum_{i=1}^{N} \tilde{s}_i \tilde{s}_i' + \mathcal{O}(\epsilon^{\phi+w_1}, \epsilon^{h+w_1}, \epsilon^{\phi+3\nu}). \tag{9}$$

Note that the external torque was transformed into a periodic forcing term using *Method 2* (*cf.* Section 2). Eq. (9) uses the pendulums' equation at first order $\tilde{s}_i'' = -n_p^2 \tilde{s}_i$ (assuming $\nu < w_1$).

Eq. (9) is similar to that obtained if the change of independent variable $t \to \tau + \Omega$ had been used. The two differences would be that $(\bullet)'$ would denote derivation with respect to $\tau + \theta$ and the torque term which would be $\tilde{T}_1 \cos[n(\tau+\theta)]$. However, using the chain rule, one can observe

$$\frac{\partial}{\partial \tau} = \frac{\partial}{\partial(\tau+\theta)} + \mathcal{O}(\epsilon^{w_1}), \quad \frac{\partial^2}{\partial \tau^2} = \frac{\partial^2}{\partial(\tau+\theta)^2} + \mathcal{O}(\epsilon^{w_1}) \tag{10}$$

so that at the order retained in Eq. (9), derivatives with respect to τ and $\tau+\theta$ are equivalent. Moreover, expanding the torque term, one can notice

$$\tilde{T}_1 \cos[n(\tau+\theta)] = \tilde{T}_1 \cos(n\tau) + \mathcal{O}(\epsilon^{r+w_1}). \tag{11}$$

This means that at the order retained in Eq. (9) and assuming $w_2 < r + w_1$, it is equivalent to transform the torque into a periodic forcing term using the change of independent variables $t \to \tau + \theta$ (*cf. Method 1* in Section 2) or assuming $\omega/\Omega \approx n$ (*cf. Method 2* in Section 2).

4.3. Pendulums' dynamics

The aim here is to uncouple the pendulums' dynamics from the rotor's. To do so, the rotor's simplified Eq. (9) is introduced in the pendulums' Eq. (1b). Then, using the trajectory and rotation functions (6) and choosing the set of scaling coefficients

$$\phi = \ell = 1, \ \nu = 1/2, \ p = q = 0, \ r = 3/2, \tag{12}$$

the pendulums' equation reduces to

$$\tilde{s}_i'' + n_p^2 \tilde{s}_i = -\epsilon \Lambda_m^{-1} \left[-2\tilde{x}_{[4]} \tilde{s}_i^3 + 6\eta \alpha_{[1]} \tilde{\alpha}_{[3]} (\tilde{s}_i^2 \tilde{s}_i'' + \tilde{s}_i \tilde{s}_i'^2) + \tilde{b} \tilde{s}_i' + \Lambda_c \left(\tilde{T}_1 \cos(n\tau) + \frac{n_p^2 \tilde{\mu} \Lambda_c}{N} \sum_{j=1}^{N} \tilde{s}_j \right) \right] + HOT. \tag{13}$$

The set of scaling parameters was chosen to uncouple the pendulums' equation from the rotor's dynamics while keeping the effect of the non-linearities coming from both the trajectory and rotation functions. Eq. (13) contains the influence of the external torque, the coupling between pendulums through the sum over N, and non-linearities coming from both the trajectory and the rotation. It is also interesting to note that because pendulums are identical and coupled, the system exhibits 1:1 internal resonances [32–34]. Eqs. (13) are weakly coupled because pendulums are coupled indirectly through the rotor and their effect on the rotor is small as their relative inertia is small [31]. Moreover, these equations are weakly non-linear because s_i were assumed small and the trajectory and rotation functions chosen (*cf.* Eq. (6)) are close to an epicycloid and a linear rotation, which render a linear behaviour for small fluctuations of the rotational speed. Note that the hypothesis and choice of scaling parameters of this study allows to investigate exclusively the effect of non-linearities due to the trajectory and rotation functions. Other sources of non-linearities, such as those arising from the coupling between the rotor and the pendulums, are missed in the present study. To account for those, other hypothesis can be made, as it is done in [3,5].

5. Solving the simplified equations and stability analysis

5.1. Application of the method of multiple scales

In the present study, the choice is made to solve the pendulums' simplified equations using the method of multiple scales [35]. Two time scales are introduced, $\tau_0 = \tau$ and $\tau_1 = \epsilon\tau$. As it was done previously for the rotor, the pendulums' displacement is expanded such that

$$\tilde{s}_i(\tau) = \tilde{s}_i^{(1)}(\tau_0, \tau_1) + \epsilon \tilde{s}_i^{(3)}(\tau_0, \tau_1) + HOT \tag{14}$$

where $\tilde{s}_i^{(1)}$ and $\tilde{s}_i^{(3)}$ represent the first and third harmonics, respectively. Inserting Eq. (14) in Eq. (13) yields a solution for $\tilde{s}_i^{(1)}$ of the form

$$\tilde{s}_i^{(1)} = a_i(\tau_1) \cos\left(n\tau_0 - \xi_i(\tau_1)\right) \tag{15}$$

where amplitudes a_i and relative phases ξ_i are governed by the $2N$ equations system

$$\begin{cases} D_1 a_i = f_{a_i}(\boldsymbol{a}, \boldsymbol{\xi}), & \text{(a)} \\ a_i D_1 \xi_i = f_{\xi_i}(\boldsymbol{a}, \boldsymbol{\xi}). & \text{(b)} \end{cases} \tag{16}$$

$\boldsymbol{a}$ and $\boldsymbol{\xi}$ are vectors containing the a_i and ξ_i, respectively, and D_1 denotes derivation with respect to τ_1. Functions f_{a_i} and f_{ξ_i} are given by

$$f_{a_i}(\boldsymbol{a}, \boldsymbol{\xi}) = -\frac{1}{2\Lambda_m n_p} \left[\Lambda_c \tilde{T}_1 \sin(\xi_i) + n_p \tilde{b} a_i + \frac{\Lambda_c^2 n_p^2 \tilde{\mu}}{N} \sum_{\substack{j=1 \\ j \neq i}}^{N} a_j \sin(\xi_i - \xi_j) \right], \tag{17a}$$

$$f_{\xi_i}(\boldsymbol{a},\boldsymbol{\xi}) = \sigma a_i - \frac{1}{2\Lambda_m n_p}\left[\Lambda_c \tilde{T}_1 \cos(\xi_i) + \frac{\Lambda_c^2 n_p^2 \tilde{\mu}}{N}\left(a_i + \sum_{\substack{j=1 \\ j\neq i}}^{N} a_j \cos(\xi_i - \xi_j)\right) - \frac{c_p}{2} a_i^3\right], \tag{17b}$$

where σ is a detuning term such that $n = n_p + \epsilon\sigma$ and c_p is a non-linear coefficient related to the perturbation of the trajectory and rotation functions. It is defined as

$$c_p = 3(\tilde{x}_{[4]} + 2n_p^2 \eta \alpha_{[1]} \tilde{\alpha}_{[3]}). \tag{18}$$

In the frame of the study led in this paper, only the steady-state regime is considered. This implies that the pendulums' amplitude and their phase relative to the excitation is time-invariant, such that

$$D_1 a_i = 0, \quad D_1 \xi_i = 0. \tag{19}$$

Introducing Eq. (19) in Eq. (16) leads to the system

$$\begin{cases} 0 = f_{a_i}(\boldsymbol{a},\boldsymbol{\xi}), & \text{(a)} \\ 0 = f_{\xi_i}(\boldsymbol{a},\boldsymbol{\xi}), & \text{(b)} \end{cases} \tag{20}$$

which is to be solved to determine the pendulums' response.

5.2. Reduction to a single mode

It was observed in Section 3 that, in a linear regime, a single mode participates to the pendulums' response. This linear mode, $\boldsymbol{\phi_{20}}$, can be called "unison mode" as it describes a motion for which all pendulums have the same amplitude and phase. As the behaviour considered in this section is weakly non-linear, it can be expected that pendulums will move at unison. Thus, it is assumed that

$$a_i = a, \quad \xi_i = \xi. \tag{21}$$

Introducing Eq. (21) in Eq. (20), one can find the following order response of pendulums at unison

$$\sigma = \frac{1}{2\Lambda_m n_p}\left[\Lambda_c^2 n_p^2 \tilde{\mu} - \frac{c_p}{2} a^2 \pm \sqrt{\Lambda_c^2 \frac{\tilde{T}_1^2}{a^2} - n_p^2 \tilde{b}^2}\right]. \tag{22}$$

The backbone of the non-linear unison mode can be deduced from Eq. (22) as $n_2 = n_p + \epsilon\ \sigma|_{\tilde{T}_1=\tilde{b}=0}$. It is interesting to note that the hardening or softening behaviour of the pendulums is governed by the sign of c_p. This property will later be used to specify design rules (*cf.* Section 7). Introducing Eq. (21) in Eq. (20), one can also find the following torque response

$$\tilde{T}_1 = \frac{a}{\Lambda_c}\left[\frac{c_p^2}{4} a^4 + 2c_p n_p \left(\Lambda_m \sigma - \frac{\Lambda_c^2}{2} \tilde{\mu} n_p\right) a^2 + 4\Lambda_m^2 n_p^2 \sigma^2 + n_p^2 \tilde{b}^2 - n_p^3 \tilde{\mu} \Lambda_c^2 \left(4\Lambda_m \sigma - \Lambda_c^2 n_p \tilde{\mu}\right)\right]^{1/2}. \tag{23}$$

Computing the amplitude response allows accessing the phase response, given by

$$\tan(\xi) = -2n_p \tilde{b}\left[4\Lambda_m n_p \sigma - 2\Lambda_c^2 n_p^2 \tilde{\mu} + c_p a^2\right]^{-1}. \tag{24}$$

Then, using the results for a and ξ and the rotor's simplified Eq. (9), one can compute the amplitude of the two first harmonics of the rotor, given by

$$\left|\tilde{\theta}^{(1)\prime\prime}\right| = \sqrt{\tilde{T}_1^2 + n_p^4 \tilde{\mu}^2 \Lambda_c^2 a^2 + 2\tilde{T}_1 n_p^2 \tilde{\mu} \Lambda_c a \cos(\xi)}, \tag{25}$$

$$\left|\tilde{\theta}^{(2)\prime\prime}\right| = \tilde{\mu} n n_t^2 a^2. \tag{26}$$

Eq. (26) highlights that non-linear effects induced by the pendulums generate higher order harmonics of the rotor (at the order retained, only the 2^{nd} harmonic, related to Coriolis effects, is present).

5.3. Stability analysis

The stability of the response is now assessed. First, system (16) can be rewritten as

$$\begin{cases} D_1 a_i = f_{a_i}(\boldsymbol{a},\boldsymbol{\xi}), & \text{(a)} \\ D_1 \xi_i = f^*_{\xi_i}(\boldsymbol{a},\boldsymbol{\xi}), & \text{(b)} \end{cases} \tag{27}$$

with $f^*_{\xi_i}(\boldsymbol{a},\boldsymbol{\xi}) = f_{\xi_i}(\boldsymbol{a},\boldsymbol{\xi})/a_i$. Then, the Jacobian of system (27) is computed and evaluated on the unison solution at steady state, yielding a $2N \times 2N$ block circulant matrix such that

$$\boldsymbol{J} = \begin{bmatrix} \boldsymbol{J_1} & \boldsymbol{J_2} & \cdots & \boldsymbol{J_2} \\ \boldsymbol{J_2} & \ddots & \ddots & \vdots \\ \vdots & \ddots & \ddots & \boldsymbol{J_2} \\ \boldsymbol{J_2} & \cdots & \boldsymbol{J_2} & \boldsymbol{J_1} \end{bmatrix}, \quad \boldsymbol{J_1} = \begin{bmatrix} \dfrac{\partial f_{a_i}}{\partial a_i} & \dfrac{\partial f_{a_i}}{\partial \xi_i} \\ \dfrac{\partial f^*_{\xi_i}}{\partial a_i} & \dfrac{\partial f^*_{\xi_i}}{\partial \xi_i} \end{bmatrix}, \quad \boldsymbol{J_2} = \begin{bmatrix} \dfrac{\partial f_{a_i}}{\partial a_j} & \dfrac{\partial f_{a_i}}{\partial \xi_j} \\ \dfrac{\partial f^*_{\xi_i}}{\partial a_j} & \dfrac{\partial f^*_{\xi_i}}{\partial \xi_j} \end{bmatrix}. \tag{28}$$

$\boldsymbol{J_1}$ represents the effect of a perturbation of the ith pendulum on itself while $\boldsymbol{J_2}$ represents the effect that a perturbation of the jth pendulums has on the ith one (with $j \neq i$). The $2N$ eigenvalues of $\boldsymbol{J}$ are given by the 2 eigenvalues of $[\boldsymbol{J_1} + (N-1)\boldsymbol{J_2}]$ and the 2 eigenvalues of $[\boldsymbol{J_1} - \boldsymbol{J_2}]$ with multiplicity $N-1$ [36]. Instabilities appear when the real part of at least one of the eigenvalues of $\boldsymbol{J}$ changes sign. The limits of the instabilities are given by

$$\det[\boldsymbol{J_1} + (N-1)\boldsymbol{J_2}] = 0, \tag{29a}$$

$$\det[\boldsymbol{J_1} - \boldsymbol{J_2}] = 0, \tag{29b}$$

and because the trace of $[\boldsymbol{J_1}+(N-1)\boldsymbol{J_2}]$ and $[\boldsymbol{J_1}-\boldsymbol{J_2}]$ is always negative, the solution is unstable when at least one of the determinants in Eq. (29) is negative.

The determinants in Eq. (29) indicate instabilities of different nature. Consider just for a moment that there is only one pendulum, i.e. $N = 1$. Then, condition (29a) reduces to $\det[\boldsymbol{J_1}] = 0$ and condition (29b) is undefined as $\boldsymbol{J_2}$ is undefined ($\boldsymbol{J_2}$ exists only when $N > 1$). For a given excitation amplitude, $\det[\boldsymbol{J_1}] = 0$ corresponds to a pair of saddle–node bifurcations between which the periodic solution is unstable. This is analogous to a classic Duffing-like bent resonance with jump phenomena [37]. By continuity, when $N > 1$, condition (29a) still indicates saddle–node bifurcations. Instabilities associated to condition (29b) arise only when several pendulums are considered, so that they are related to a loss of unison [4]. Thus, for a given excitation amplitude, condition (29b) corresponds to a pair of pitchfork bifurcations between which the pendulums' response is localised on one or more pendulums.

The critical pendulums' amplitudes corresponding to saddle–node bifurcations are the solutions of condition (29a) and are given by

$$a_{sn} = \sqrt{\frac{-8\sigma\Lambda_m n_p + 4\Lambda_c^2 n_p^2\tilde{\mu} \pm 2n_p\sqrt{\left(2\sigma\Lambda_m - n_p\Lambda_c^2\tilde{\mu}\right)^2 - 3\tilde{b}^2}}{3c_p}}. \tag{30}$$

Similarly, the critical pendulums' amplitudes corresponding to pitchfork bifurcations are the solutions of condition (29b) and are given by

$$a_{pf} = \sqrt{\frac{-8\sigma\Lambda_m n_p \pm 2n_p\sqrt{4\sigma^2\Lambda_m^2 - 3\tilde{b}^2}}{3c_p}}. \tag{31}$$

These critical amplitudes are depicted in Fig. 3. It is interesting to note that the critical amplitudes a_{sn} and a_{pf} tend to infinity as c_p tends to zero. This observation will come useful in Section 7. Moreover, the critical amplitudes are independent of the forcing amplitude $\tilde{T}_1$.

5.4. Limits of the model

It is of importance to bear in mind that the previous analytical computations involve assumptions that limit the range of validity of the model. One of the approximations of the non-linear model is exposed in details below and an order of magnitude of the non-dimensional parameters that can be used in the model is given. The backbone of the unison mode (*cf.* Section 5.2) evaluated for zero pendulums' displacement is a Taylor expansion of the linear eigenvalue n_{20} (*cf.* Eq. (3)) with respect to μ such that

$$n_{20} = \underbrace{n_p + \mu\frac{n_p\Lambda_c^2}{2\Lambda_m}}_{\text{backbone at } a=0} + \mu^2\frac{n_p}{8}\frac{\Lambda_c^2}{\Lambda_m}\left(3\frac{\Lambda_c^2}{\Lambda_m} - 4\right) + \mathcal{O}(\mu^3), \tag{32}$$

where the backbone contains only the two first terms. For the analytical model to be accurate, one needs the third term to be negligible. Eq. (32) allows to write an approximated condition on μ such that the relative error on the backbone at $a = 0$ does not exceed 100χ %. It is given by

$$\mu < \frac{\chi + \sqrt{\chi^2 + 8\chi\left|\frac{3}{4} - \frac{\Lambda_m}{\Lambda_c^2}\right|}}{2\left|\frac{3\Lambda_c^2}{4\Lambda_m} - 1\right|}. \tag{33}$$

In Section 4.1, μ was proposed as the small perturbation parameter of the perturbation analysis. Thus, one can chose $\mu = \epsilon$, yielding an order of magnitude not to be overpassed for every small parameter.

6. Case study and numerical validation

The former developments are now applied on a system of two pendulums. The aim is to present the main assets of the analytical model and to compare them with an exact (numerical) resolution of the equations of motion (1a) and (1b) as a first validation. To perform the numerical resolution, the change of independent variable $\tau \to \tau + \theta$ is introduced in Eqs. (1a) and (1b) to transform the torque into a periodic forcing term while keeping the equations exact (*cf. Method 1* in Section 2). Two different numerical resolutions are used in this paper:

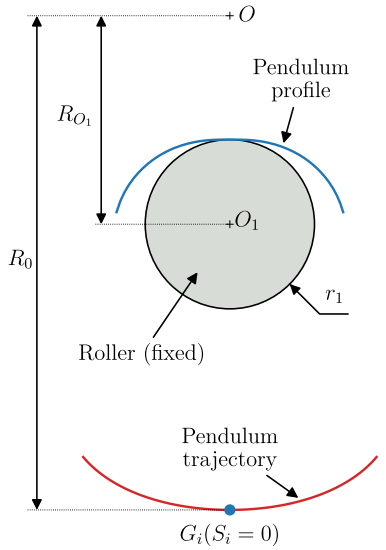

Fig. 2. CPVA studied (only one of the two pendulums is represented, the architecture being symmetric).

Table 1
Parameters of the CPVA studied in this section.

N	n_p	η	μ	$x_{[4]}$	$\alpha_{[1]}$	$\alpha_{[3]}$	$\bar{b}$	$\bar{b}_r$
2	0.5	1.4	0.1	−4.2	1.33	0.06	0.16	0.002

- The equations are integrated numerically using a Runge–Kutta algorithm until the steady state is reached. Then, the signals' amplitudes are obtained through a decomposition into Fourier series.
- The equations are solved with MANLAB, which is a path-following and bifurcation analysis software [38].

The CPVA studied in this section is represented in Fig. 2 and its parameters are given in Table 1. Its low tuning order ($n_p = 0.5$) makes it well suited for filtering out vibrations arising from cylinders deactivation. The CPVA is made of two monofilar pendulums (only one is represented in Fig. 2). The profile of a pendulum rolls without slipping on a roller of radius r_1 (fixed on the rotor). The shape of the profile allows to control the trajectory followed by the pendulum's centre of mass. For such pendulums, the rotation function $\alpha(s_i)$ is governed by the functional geometry. The two first rotation coefficients are

$$\alpha_{[1]} = \frac{R_0}{R_0 - R_{O_1} + r_1}, \tag{34}$$

$$\alpha_{[3]} = \alpha_{[1]} \frac{R_{O_1}\left(1+n_t^2\right)^2 - R_0 n_t^2\left(1+n_t^2\right) - \alpha_{[1]} R_{O_1}\left(1+n_t^2\right) + \alpha_{[1]} R_0 n_t^2}{6\left(R_{O_1} - R_0 + \alpha_{[1]} R_0^{-1}\left(\left(R_0 - R_{O_1}\right)^2 - r_1^2\right)\right)}. \tag{35}$$

6.1. Evaluation of the stability as function of mistuning

In practice, the excitation order is fixed such that $n = cte$. However, pendulums may not be tuned exactly to the excitation. This mistuning can be intentional or may arise from material imperfections. Either way, varying the excitation order is similar to introducing mistuning (provided that pendulums are equally mistuned) and is therefore relevant for studying the effect of mistuning on the system's response [8]. The order response of pendulums at unison and their stability is shown in Fig. 3 for several torque amplitudes. The bending of the response indicates that pendulums exhibit a hardening behaviour. The bifurcation zones (unstable unison in red and unstable periodic response in blue), delimited by the bifurcation curves (30) and (31), are shown. The zone corresponding to simultaneous unstable unison and unstable periodic responses is represented in purple while stable responses are represented in green. The same colour code will be used throughout this paper. For small torque amplitudes, the response is almost linear so that no stability changes will occur. As the torque amplitude is increased, the unison response crosses the bifurcation curves, leading to a different stability state.

6.2. Visualisation of the stability in the design space

An original visualisation of the pendulums' stability in the design space is now presented. This space allows to assess the stability of pendulums of the same type but with different sets of parameters $(x_{[4]}, \alpha_{[1]}, \alpha_{[3]})$. In the general case, it is thus a 3D space. However,

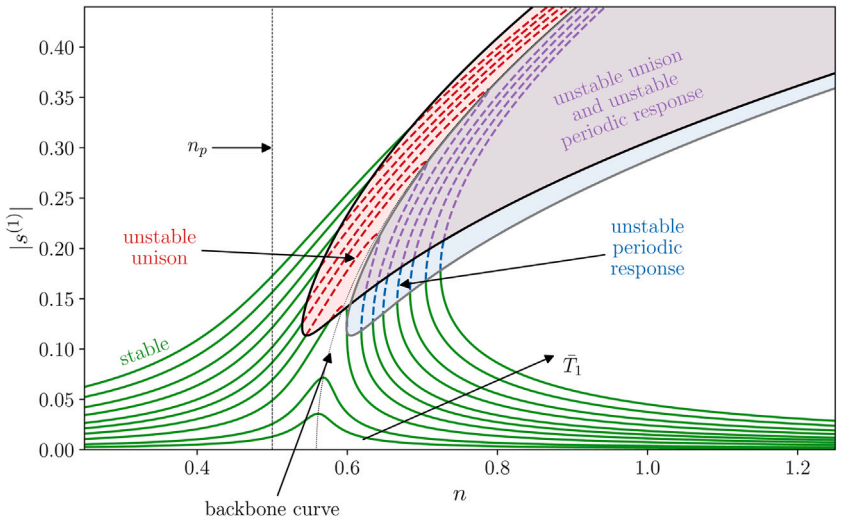

Fig. 3. Order response of the pendulums at unison and their stability. Portions of the response curves corresponding to stable unison, unstable unison and unstable periodic responses are represented in green, red and blue, respectively. Portions where both the unison and the periodic response are unstable are represented in purple. Additionally, all unstable portions are shown as dashed-lines. The black and grey curves represent the pitchfork and saddle–node bifurcations, respectively. $\bar{T}_1 = \{0.1, 0.2, 0.4, 0.6, 0.8, 1, 1.3, 1.6, 2, 2.4\} \times 10^{-2}$.

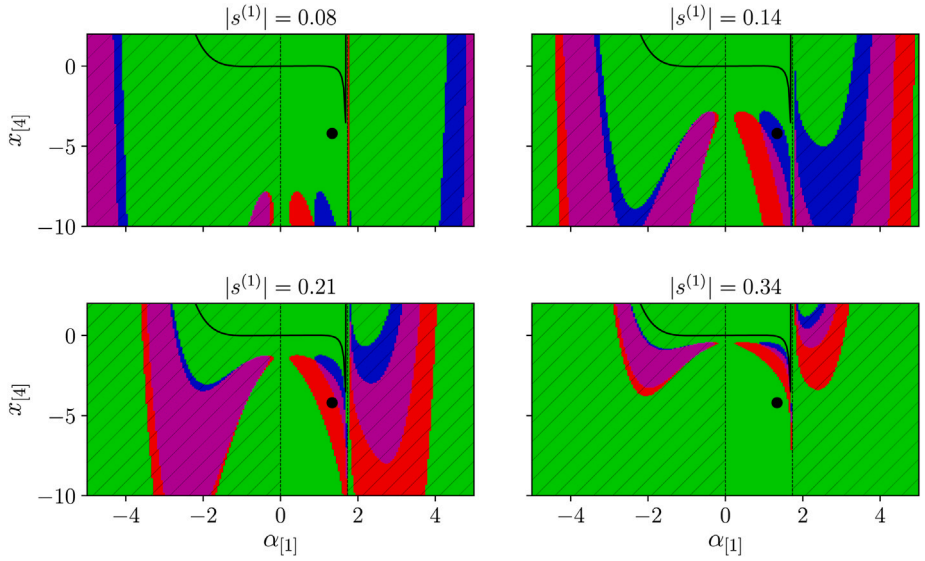

Fig. 4. Representation of the stability in the design space $(\alpha_{[1]}, x_{[4]})$. The colour code is the same as that used in Fig. 3, so that areas corresponding to stable unison, unstable unison and unstable periodic responses are represented in green, red and blue, respectively. Areas where both the unison and the periodic response are unstable are represented in purple. The black dot corresponds to the design represented in Fig. 3. The black curve represents designs rendering a linear behaviour. The hatched regions indicate non-achievable designs. $n = 0.63$, $R_{O_1}/R_0 = 0.422$. (For interpretation of the references to colour in this figure legend, the reader is referred to the web version of this article.)

for the CPVA presented in Fig. 2, the rotation is imposed by the functional geometry causing $\alpha_{[3]}$ to be related to $\alpha_{[1]}$. Moreover, due to space constraints, it is convenient to evaluate designs for a fixed value of the ratio R_{O_1}/R_0. Thus, using Eqs. (34) and (35), one can get $\alpha_{[3]}$ as a function of $\alpha_{[1]}$, which reduces the design space to a 2D space. This method is used to represent the stability of pendulums of the same type as that depicted in Fig. 2 under the form of maps, shown in Fig. 4. Each map is represented for a given amplitude and a given excitation order. Colours represent the stability (the colour code is the same as that used previously). The black line represents designs for which the values of $x_{[4]}$, $\alpha_{[1]}$ and $\alpha_{[3]}$ render the system linear (*cf.* Section 7). The meaning of the hatched regions will be defined later. The black dot corresponds to the design shown in Fig. 3 so that it is fixed in the design space. This specific design passes through several stability states as the amplitude of motion increases. This could already be observed looking at Fig. 3 for $n = 0.63$. The purpose of the representation in the design space is to identify designs which are likely or not

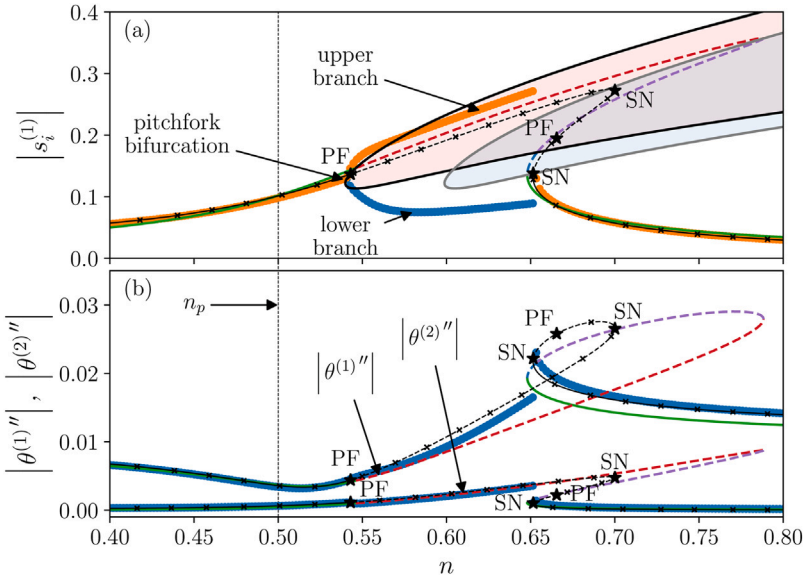

Fig. 5. Comparison of the pendulums' response (a) and rotor's response (b) obtained analytically and numerically. The colour code of the analytical results is the same as that used in Fig. 3. Circles represent the numerical results obtained through temporal integrations. In (a), one of the pendulums is represented by blue circles, the other by orange ones. The MANLAB solution is given as a black line with cross markers. Bifurcation points found with MANLAB are marked as black stars with an associated code name. Code names "PF" and "SN" refer to "pitchfork" and "saddle–node" bifurcations, respectively. $\bar{T}_1 = 0.01$.

to exhibit instabilities. For instance, the upper central region delimited by the black curve on the maps remains stable over the amplitude range represented. This remark will be further discussed in Section 7. Note that there seems to be an artefact on the maps around $\alpha_{[1]} = 1.7$. However, this simply corresponds to a value of $\alpha_{[1]}$ for which r_1 tends to zero, causing $\alpha_{[3]}$ to tend to ∞. Above this threshold value of $\alpha_{[1]}$, r_1 is negative, which is non-physical (remind that r_1 is a radius so that it should not be negative). Similarly, r_1 is negative for $\alpha_{[1]} < 0$. The hatched regions thus correspond to non-achievable designs.

6.3. *Comparison with a numerical model*

In this section, the analytical model is compared with an exact resolution of Eqs. (1a) and (1b). The pendulums' response obtained through the analytical and numerical models is presented in Fig. 5(a). Like what was observed in the case of absorbers with a pure translation motion [8], the unison mode looses its stability through a pitchfork bifurcation in favour of a localised response. The bifurcation point, theoretically located at the intersection of the black curve and the unison response, is accurately predicted by the model. After this bifurcation, the response divides into two branches so that energy is localised on one of the two pendulums. The pendulum located on the upper branch has a larger amplitude of motion than that predicted by the unison mode, which can be an issue as the maximum amplitude is limited by the nature of the trajectory chosen. This being said, one can see in Fig. 5(a) that the upper branch is close to the (unstable) unison response. Thus, in the case considered here, the risk of reaching the maximum amplitude is not significantly increased by the localisation. The jump located at $n \approx 0.65$ is also well predicted by the model. The amplitude of the stable solution is very well predicted by the analytical model. However, comparing with the MANLAB results, one can see that the analytical model overestimates the unstable solution. Similarly, the bifurcation points located on the unstable solution are not well predicted (especially the saddle–node bifurcation, which is theoretically located at the right intersection of the grey curve and the unison response, around $n \approx 0.69$). The reason for those discrepancies is that the amplitude on the unstable solution is rather large, so that some of the non-linear terms that were dropped in the analytical model have a non-negligible effect. Moreover, the analytical solution is based on a perturbation method around $n = n_p$ (*cf.* Section 5.1), so that less accuracy can be expected as n departs from n_p. This being said, an accurate prediction of the stable solution and the two bifurcation points at $n \approx 0.54$ and $n \approx 0.65$ is the most important point, as only those will be observed in practice. The difference both in phase and amplitude of the pendulums' localised responses is visible on the temporal signals given in Fig. 6(a).

Fig. 5(b) shows a comparison of the rotor's response obtained through the analytical and numerical models. Again, the analytical model allows an accurate prediction of the rotor's response on its stable (green) portions. Surprisingly, portions for which pendulums are not in unison are also well predicted by the model, even though the model uses only the unison mode. This is an interesting point, as it tends to show that localisation does not necessarily impact the rotor's dynamics. Looking at the response of $\theta^{(1)}$, one can see that the non-linearity shifted the antiresonance so that it does not correspond to the linear tuning order n_p. This problem is considered in [39]. The distortion of θ'' coming from the presence of $\theta^{(2)}$ (and in a smaller amount, higher harmonics), can be seen in Fig. 6(b).

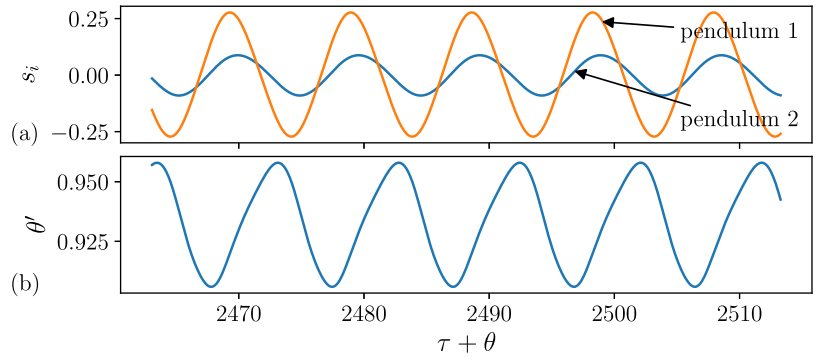

Fig. 6. Temporal signals (truncated) of the pendulums (a) and rotor (b) obtained through a numerical integration of the equations of motion. These signals lead to the amplitudes shown in Fig. 5 at $n = 0.65$.

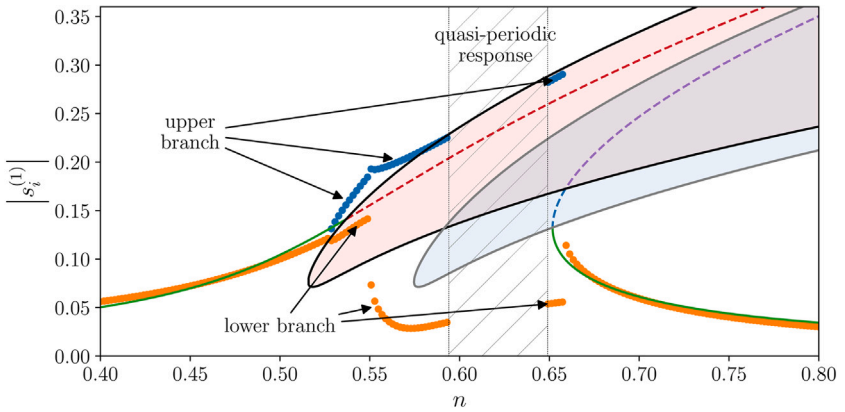

Fig. 7. Pendulums' order response exhibiting non-periodic localised solutions. The colour code of the analytical results is the same as that used in Fig. 3. Circles represent the numerical results. One of the pendulums is represented by blue circles, the other by orange ones. $\bar{b} = 0.063$, $\bar{T}_1 = 0.01$. (For interpretation of the references to colour in this figure legend, the reader is referred to the web version of this article.)

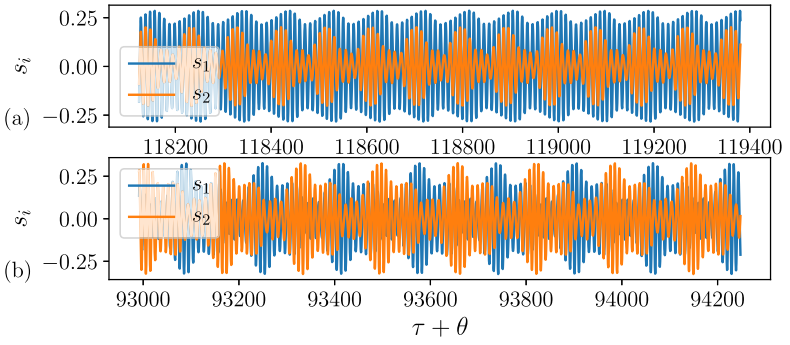

Fig. 8. Temporal signal (truncated) of the pendulums obtained through a numerical integration of the equations of motion. These signals correspond to the quasi-periodic portion of Fig. 7 at (a) $n = 0.621$ and (b) $n = 0.631$.

Other sets of system parameters can lead to solutions more complicated than the ones presented in Fig. 5. For instance, Fig. 7 shows the pendulums' response for a smaller damping than previous simulations, but unchanged other parameters. As in Fig. 5, the response divides into branches through a pitchfork bifurcation. In Fig. 7, those branches are broken into three parts. Localised responses might be subject to instabilities such as jumps of the response [6,7], which explains the discontinuity observed around $n = 0.55$. Between $n \approx 0.59$ and $n \approx 0.65$, no numerical results are shown because the corresponding time signals are not periodic. Two of those temporal signals are represented in Fig. 8. Fig. 8(a) shows a solution for which energy localisation is visible but the amplitude of the two pendulums is modulated. Such quasi-periodic solutions appear through Neimark-Sacker bifurcations [8].

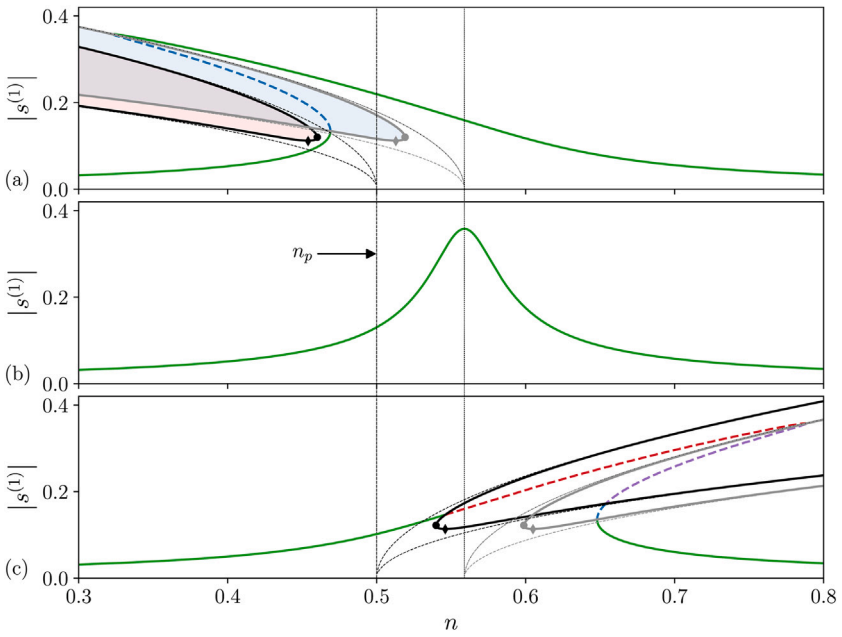

Fig. 9. Behaviour of the response according to the value of $x_{[4]}$. (a) softening, $x_{[4]} = 4.2$, (b) linear, $x_{[4]} = -0.0561$, (c) hardening, $x_{[4]} = -4.2$. The limits of the bifurcation zones in the undamped case are represented with dashed lines. $\bar{T}_1 = 0.01$ and system parameters are given in Table 1. The colour code is the same as that used in Fig. 3. The black and grey dots indicate the points corresponding to $n_d^{(v)}$ and $n_j^{(v)}$, respectively. The black and grey diamonds indicate the points corresponding to $n_d^{(h)}$ and $n_j^{(h)}$, respectively.

The quasi-periodic solution represented in Fig. 8(b) seems to highlight energy exchanges between the two pendulums, causing the response to be localised successively on each pendulum.

7. Design rules

As discussed in the previous sections, the expected unison motion of pendulums can be broken in favour of more complex regimes. When it arises, desynchronisation leads to an undesired behaviour where one or more pendulums oscillate with an amplitude larger than if they were at unison. This might decrease the efficiency of the vibration absorption and it can lead to impact noise issues if the pendulums hit their cusp point. Additionally, impact non-linearities would greatly change the dynamics of the system. This section proposes several design rules allowing to avoid instabilities of the system.

As seen in Section 5.2, the hardening or softening behaviour of the pendulums is governed by the sign of c_p. Setting this coefficient to zero renders the pendulums' response linear (*cf.* Eqs. (22) and (23)) so that the limits of the instability zones tend towards infinity (*cf.* Eqs. (30) and (31)). Thus, the design rule

$$c_p = 0 \quad \Leftrightarrow \quad x_{[4]} = -2\eta\alpha_{[1]}\alpha_{[3]}n_p^2 \tag{36}$$

is proposed. Physically, this rule means that the non-linearities coming from the trajectory and rotation counterbalance to render the system almost linear. The only non-linearity remaining is that related to Coriolis effects in the rotor's Eq. (9) which generates $\theta^{(2)}$ [40]. Note that the special case $x_{[4]} = \alpha_{[3]} = 0$ is that studied in Section 3: it corresponds to an epicycloidal trajectory and a linear rotation function.

Relation (36) is represented by a black line in the maps of Figs. 4 and 10. The inner region delimited by this line corresponds to softening behaviours whilst the outer region corresponds to hardening ones. For large amplitudes of motion, the instability regions tend to embrace the black curve. This interesting remark will be discussed later in this section. Eq. (36) is also represented in Fig. 9, along with other values of $x_{[4]}$ yielding softening and hardening behaviours.

If Eq. (36) cannot be fulfilled, other recommendations can be proposed. These recommendations use the vertical and horizontal tangents of the bifurcation curves (30) and (31), whose corresponding orders are given by

$$n_j^{(v)} = n_2\big|_{a=0} \pm \frac{\bar{b}\sqrt{3}}{2\Lambda_m}, \quad n_j^{(h)} = n_2\big|_{a=0} \pm \frac{\bar{b}}{\Lambda_m}, \quad n_d^{(v)} = n_p \pm \frac{\bar{b}\sqrt{3}}{2\Lambda_m}, \quad n_d^{(h)} = n_p \pm \frac{\bar{b}}{\Lambda_m}. \tag{37}$$

Subscripts j and d are related to the jumps and the desynchronisation of the response, respectively. Superscripts v and h indicate a vertical and horizontal tangent, respectively. + and − solutions correspond to hardening and softening behaviours, respectively. $n_2\big|_{a=0}$ is the backbone of the unison mode evaluated for zero pendulums' displacement (*cf.* Eq. (22)). Points corresponding to Eq. (37)

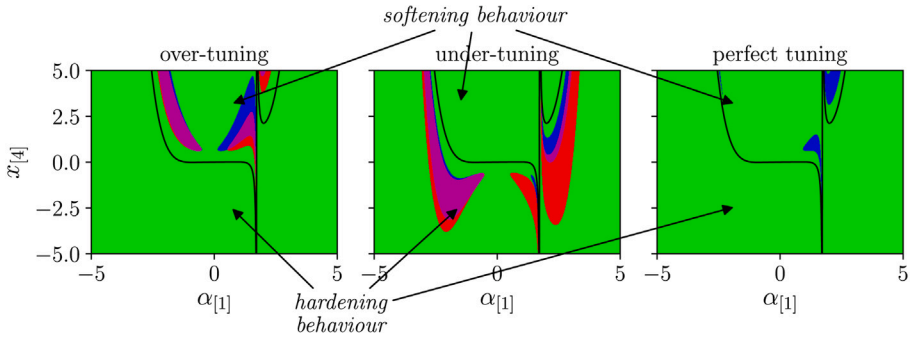

Fig. 10. Representation of the stability in the design space $(\alpha_{[1]}, x_{[4]})$ for three different tuning levels: $n = 0.4$ (over-tuning), $n = 0.6$ (under-tuning) and $n = 0.5$ (perfect tuning). The other system parameters are given in Table 1. The colour code is the same as that used in Fig. 3. The black curve represents designs rendering a linear behaviour. Each map is represented for $|s^{(1)}| = 0.3$ and $R_{O_1}/R_0 = 0.422$.

are represented with black and grey dots and diamonds in Fig. 9. Vertical tangents indicate the minimum level of mistuning for the response to become unstable whilst horizontal tangents indicate the minimum amplitude for which the response enters into an instability zone. Note that the torque level corresponding to these tangents can be obtained using Eqs. (37), (30), (31), and (23). Looking at the vertical tangents, one can see that in the hardening case, $n_p < n_d^{(v)} < n_j^{(v)}$, whilst in the softening case, $n_d^{(v)} < n_p < n_j^{(v)}$ or $n_d^{(v)} < n_j^{(v)} < n_p$. This means that hardening pendulums do not exhibit instabilities as long as $n \leq n_p$ (i.e. they are perfectly tuned or over-tuned). Similarly, softening pendulums do not exhibit unison instabilities as long as $n \geq n_p$ (i.e. they are perfectly tuned or under-tuned). These softening pendulums are however very likely to be subject to jumps even if they are perfectly tuned or under-tuned. This happens if $n_j^{(v)} > n_p$, which is the case in general as damping is small. These remarks are illustrated in Fig. 9 where one can see that the limit of the non-unison zones (black curves) do not cross the vertical line $n = n_p$, whilst the limit of the unstable periodic response (grey curves) crosses it in the softening case. These results are consistent with those obtained considering purely translated undamped pendulums [7]. Moreover, one can see from Eq. (37) that $n_d^{(v)}$ and $n_d^{(h)}$ tend to n_p as damping is reduced. In other words, the small-damping configuration is the most critical one as a very small level of mistuning can lead to a loss of unison. Similarly, $n_j^{(v)}$ and $n_j^{(h)}$ tend to $n_2|_{a=0}$ as damping is reduced. This is visible in Fig. 9, where the limit of the instability zones corresponding to the undamped case are represented with dashed lines.

As remarked previously, the maps presented in Fig. 4 show that the instability regions tend to embrace the black line corresponding to Eq. (36) without crossing it. The situation depicted in those maps corresponds to $n_p < n$, with n sufficiently large so that only hardening pendulums exhibit instabilities, which explains why the instability regions are contained in the outer zone delimited by the black line. Moreover, the instability regions tend towards the black line because, for large amplitudes of motion, the response can be unstable only if the critical amplitudes described by Eqs. (30) and (31) are large. These critical amplitudes get higher as the non-linearity reduces, thus explaining why the instability regions approach the black line at large amplitudes of motion. Indeed, one can see that as $c_p \to 0$, the critical amplitudes a_{pf} and a_{sn} (*cf.* Eqs. (30) and (31)) tend to infinity.

Three different tuning levels (over-tuning, under-tuning and perfect tuning of the pendulums) are represented in the design space in Fig. 10 to illustrate the former developments. For over-tuned pendulums, the instability regions are contained in the inner zone delimited by the black curve. For largely under-tuned pendulums, these instability zones are limited to the outer region delimited by the black curve. Finally, for a perfect tuning, only softening pendulums can be subject to jumps.

8. Experimental validation

An experimental study on the CPVA displayed in Fig. 11 was led to assess the accuracy of the analytical and numerical results. This CPVA is that presented in Fig. 2. It is composed of two identical monofilar pendulums designed especially to exhibit energy localisation. The expanded shape of the pendulums aims at increasing their inertia, thus increasing the impact of rotation. The experimental setup is shown in Fig. 12. The rotor is fixed on a bench of inertia J_b using an adaptation system of inertia J_a. Thus, J_r has to be replaced by the equivalent inertia $J_{eq} = J_r + J_b + J_a$ in the previous developments. The pendulums' amplitude of motion was obtained experimentally as follows:

1. Markers are placed at the pendulums' mass centres.
2. The CPVA is centrifugated and an oscillating torque is applied through the actuator while a fast camera records a movie of the rotating system.
3. The movie recorded is decomposed into frames and each frame is rotated by the opposite of the rotor's angular position. As a consequence, those rotated frames form a movie in which the rotor's position is fixed.
4. A point-tracking algorithm is used to find the position of the pendulums' mass centres. Repeating this operation for each rotated frame yields two time signals corresponding to the two pendulums' positions.
5. The time signals are decomposed into Fourier series to extract the pendulums' amplitudes.

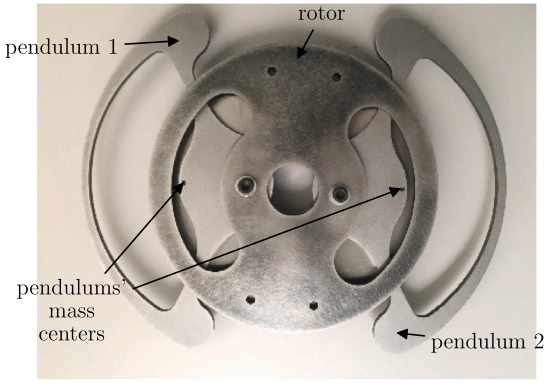

Fig. 11. CPVA used for the experiments.

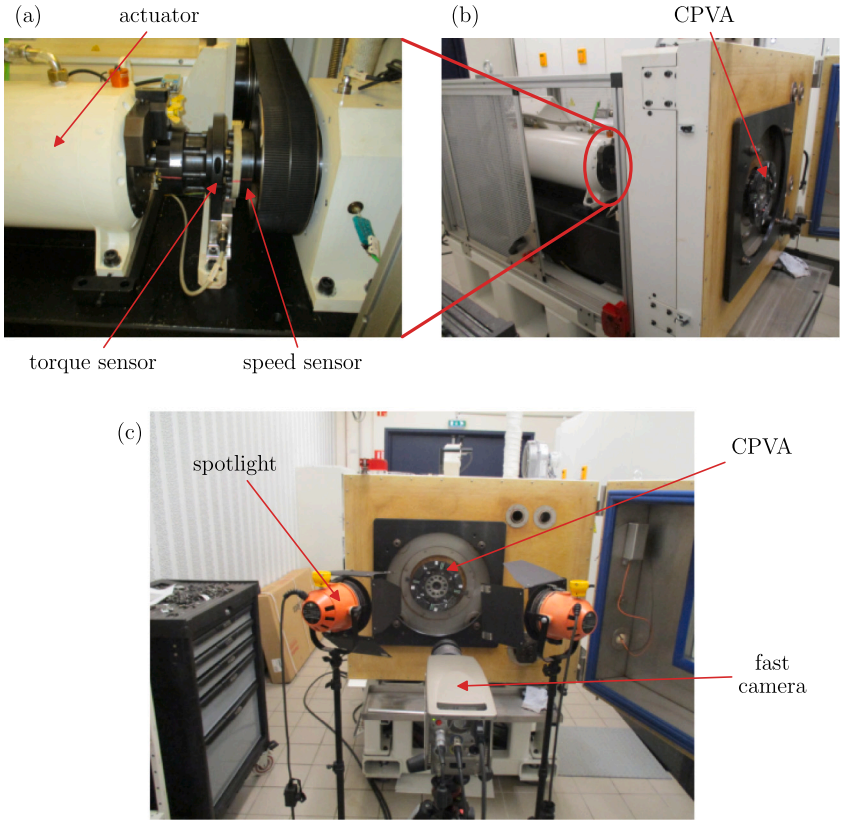

Fig. 12. Experimental setup. (a) zoom on a side view, (b) global view, (c) front view. Note that the CPVA shown in this figure is not the one used for the experiments.

Table 2
Parameters of the CPVA studied experimentally.

N	n_p	η	$x_{[4]}$	$\alpha_{[1]}$	$\alpha_{[3]}$	μ	$\bar{b}$	$\bar{b}_r$
2	0.5	0.88	−4.2	1.33	−0.02	0.167	0.043	0.002

This procedure was repeated for four torque amplitudes, $T_1 = \{3, 6, 10, 12\}$ [Nm], and for $n = 0.568$ and $\Omega = 1500$ [rpm]. The damping coefficients of the CPVA are found experimentally. The parameters of the system are given in Table 2.

A comparison of the experimental results with the analytical and numerical models is shown in Fig. 13. For $T_1 = \{3, 6\}$ [Nm], the pendulums' amplitudes obtained experimentally are significantly different. This indicates energy localisation, in accordance with the analytical and numerical solutions. The accuracy of the localised branches obtained numerically is not extremely good as the

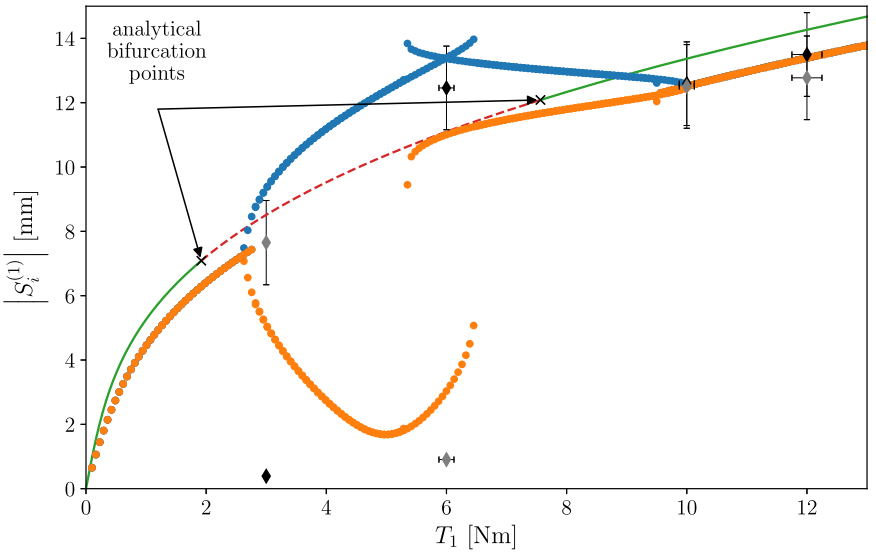

Fig. 13. Comparison of the analytical, numerical and experimental results. Blue and orange circles represent the numerical results (obtained with increasing and decreasing torque sweeps). Diamonds represent the experimental results. One of the pendulums is represented by black diamonds, the other by grey ones. The curve represents the analytical results (stable in green, unstable unison in red). Black crosses indicate the bifurcation points obtained analytically. $n = 0.568$, $\Omega = 1500$ [rpm].

diamonds do not superimpose on the circles. Regarding the upper branch, the difference between the experimental and numerical points almost falls within the measurement errors. However, the difference between numerical and experimental points on the lower branch is rather large. This is mainly due to the fact that, for very small amplitudes, the records of the pendulums' time signals had a low signal to noise ratio, so that the decomposition into Fourier series was inaccurate. This is the reason why no uncertainties along $\left|S_i^{(1)}\right|$ are shown for the two lower points. The discontinuities on the localised branches observed around $T_1 = 5.3$ [Nm] and $T_1 = 6.5$ [Nm] is due to a jump of the response, as observed previously in Fig. 7. The measurement points at $T_1 = \{10, 12\}$ [Nm] agree well with the numerical results. The slight difference of amplitude on the last measurement point is not attributed to a non-linear phenomenon but to measurement errors coming from different sources. The main sources of errors of the experimental results are listed below:

- The torque and speed regulation of the bench do not allow for an exact control of T_1 and Ω. Thus, their values are always slightly different from the prescribed ones.
- Because of manufacturing tolerances and material defects, the geometry of the system cannot perfectly match the prescribed one. Thus, the effective parameters of the system are not exactly those given in Table 2 and the two pendulums are not rigorously identical.
- The point-tracking algorithm requires bright images to accurately find the pendulums' mass centres. Despite the use of spotlights, the images obtained were rather dark.
- The markers used by the point-tracking algorithm are stickers placed by hand as closely as possible to the pendulums' mass centres shown in Fig. 11. The point-tracking algorithm looks for the centre of the markers, which are unlikely to perfectly overlap the mass centres.
- The expected motion is a rolling without slipping of the pendulum profile on the roller. However, because of the almost-flat shape of the middle of the pendulums' profile (see Fig. 2), the odds of slipping when the S_i pass through zero are not insignificant.
- The steady-state regime can take some time to be reached, especially when one expects non-linear behaviours such as localisation. It is possible that some movies were recorded before the steady-state is completely established.

The analytical model, though giving very good qualitative results (localisation is found where expected), slightly overestimates the amplitude at unison and predicts both bifurcation points too early. This highlights limits of the model, which were discussed in Sections 5.4 and 6.3 .

9. Conclusion

The study presented in this paper deals with the stability of centrifugal pendulum vibration absorbers (CPVA) allowing a rotational mobility. Stabilities of two different natures are considered. The instability of the unison response leads to a response localised on one of the pendulums. The instability of the periodic solution leads to a jump of the response. An analytical model

allowing for the prediction of these instabilities was build using a scaling of the parameters, the method of multiple scales and a reduction to a single mode. This model was validated with both numerical and experimental results. An original visualisation of the stability in the design space was presented. This allowed a simultaneous stability assessment of pendulum designs. Moreover, a design rule rendering the pendulums' behaviour linear was proposed. In case this rule cannot be applied, other recommendations were advised. These dealt with the largest mistuning levels leaving the response free of instabilities. Results were interpreted dividing the pendulums in two categories: those exhibiting hardening behaviours and those exhibiting softening ones. Hardening pendulums are stable if they are perfectly or over-tuned. Regarding softening pendulums, the stability of the unison response is preserved as long as they are perfectly or under-tuned. However, jumps can occur whether they are over or under-tuned. Finally, increasing the damping enlarges the range of mistuning for which instabilities are avoided.

CRediT authorship contribution statement

V. Mahe: Formal analysis, Investigation, Validation, Writing – original draft, Investigation, Methodology, Conceptualization, Software. **A. Renault:** Supervision, Conceptualization, Resources, Writing – review & editing. **A. Grolet:** Supervision, Validation, Visualization, Writing – review & editing. **O. Thomas:** Supervision, Validation, Visualization, Writing – review & editing. **H. Mahe:** Supervision, Resources, Funding acquisition.

Declaration of competing interest

The authors declare that they have no known competing financial interests or personal relationships that could have appeared to influence the work reported in this paper.

References

[1] D.E. Newland, Nonlinear problems of centrifugal pendulum vibration absorbers, in: Mechanisms and Machines, Vol. 1, Varna (Bulgaria), 1965.
[2] H.H. Denman, Tautochronic bifilar pendulum torsion absorbers for reciprocating engines, J. Sound Vib. 159 (2) (1992) 251–277, http://dx.doi.org/10.1016/0022-460X(92)90035-V.
[3] C.-P. Chao, S. Shaw, C.-T. Lee, Stability of the unison response for a rotating system with multiple tautochronic pendulum vibration absorbers, J. Appl. Mech. 64 (1) (1997) 149–156, http://dx.doi.org/10.1115/1.2787266.
[4] A.S. Alsuwaiyan, S.W. Shaw, Performance and dynamic stability of general-path centrifugal pendulum vibration absorbers, J. Sound Vib. 252 (5) (2002) 791–815, http://dx.doi.org/10.1006/jsvi.2000.3534.
[5] S.W. Shaw, B. Geist, Tuning for performance and stability in systems of nearly tautochronic torsional vibration absorbers, J. Vib. Acoust. 132 (4) (2010) http://dx.doi.org/10.1115/1.4000840.
[6] A.S. Alsuwaiyan, S.W. Shaw, Non-synchronous and localized responses of systems of identical centrifugal pendulum vibration absorbers, Arab. J. Sci. Eng. 39 (12) (2014) 9205–9217, http://dx.doi.org/10.1007/s13369-014-1464-1.
[7] J.S. Issa, S.W. Shaw, Synchronous and non-synchronous responses of systems with multiple identical nonlinear vibration absorbers, J. Sound Vib. 348 (2015) 105–125, http://dx.doi.org/10.1016/j.jsv.2015.03.021.
[8] A. Grolet, A. Renault, O. Thomas, Energy localisation in periodic structures: application to centrifugal pendulum vibration absorber, in: International Symposium on Transport Phenomena and Dynamics of Rotating Machinery, Maui (Hawaii), 2017.
[9] K. Nishimura, T. Ikeda, Y. Harata, Localization phenomena in torsional rotating shaft systems with multiple centrifugal pendulum vibration absorbers, Nonlinear Dynam. 83 (3) (2016) 1705–1726, http://dx.doi.org/10.1007/s11071-015-2441-2.
[10] A. Renault, Calcul et optimisation d'absorbeurs pendulaires dans une chaîne de traction automobile [Simulation and optimisation of pendular absorbers for automotive powertrain], (Ph.D. thesis), ENSAM, Lille, 2018.
[11] H. Mahé, A. Renault, O. Thomas, Dispositif d'amortissement Pendulaire [Pendular Damping Device], 2018, FR 3 055 037.
[12] H. Mahé, A. Renault, O. Thomas, Dispositif d'amortissement pendulaire [pendular damping device], 2018, FR 3 055 038.
[13] M.A. Acar, Design and tuning of centrifugal pendulum vibration absorbers, (Ph.D. thesis), Michigan State University, Michigan, 2017.
[14] J. Mayet, H. Ulbrich, Tautochronic centrifugal pendulum vibration absorbers: General design and analysis, J. Sound Vib. 333 (3) (2014) 711–729, http://dx.doi.org/10.1016/j.jsv.2013.09.042.
[15] M. Cirelli, J. Gregori, P. Valentini, E. Pennestrí, A design chart approach for the tuning of parallel and trapezoidal bifilar centrifugal pendulum, Mech. Mach. Theory 140 (2019) 711–729, http://dx.doi.org/10.1016/j.mechmachtheory.2019.06.030.
[16] M. Cirelli, M. Cera, E. Pennestrì, P.P. Valentini, Nonlinear design analysis of centrifugal pendulum vibration absorbers: An intrinsic geometry-based framework, Nonlinear Dynam. 102 (3) (2020) 1297–1318, http://dx.doi.org/10.1007/s11071-020-06035-1.
[17] M. Cera, M. Cirelli, E. Pennestrì, P. Valentini, The kinematics of curved profiles mating with a caged idle roller - higher-path curvature analysis, Mech. Mach. Theory 164 (2021) 104414, http://dx.doi.org/10.1016/j.mechmachtheory.2021.104414.
[18] M. Cera, M. Cirelli, E. Pennestrì, P.P. Valentini, Design analysis of torsichrone centrifugal pendulum vibration absorbers, Nonlinear Dynam. 104 (2) (2021) 1023–1041, http://dx.doi.org/10.1007/s11071-021-06345-y.
[19] M. Cera, M. Cirelli, E. Pennestrì, P.P. Valentini, Nonlinear dynamics of torsichrone CPVA with synchroringed form closure constraint, Nonlinear Dynam. (2021) http://dx.doi.org/10.1007/s11071-021-06732-5.
[20] M. Cirelli, E. Capuano, P.P. Valentini, E. Pennestrì, The tuning conditions for circular, cycloidal and epicycloidal centrifugal pendula: A unified cartesian approach, Mech. Mach. Theory 150 (2020) 103859, http://dx.doi.org/10.1016/j.mechmachtheory.2020.103859.
[21] J. Mayet, H. Ulbrich, First-order optimal linear and nonlinear detuning of centrifugal pendulum vibration absorbers, J. Sound Vib. 335 (2015) 34–54, http://dx.doi.org/10.1016/j.jsv.2014.09.017.
[22] X. Tan, S. Yang, J. Yang, J. Li, Study of dynamics of rotational centrifugal pendulum vibration absorbers based on tautochronic design, Meccanica (2021) http://dx.doi.org/10.1007/s11012-021-01340-4.
[23] E.R. Gomez, I.L. Arteaga, L. Kari, Normal-force dependant friction in centrifugal pendulum vibration absorbers: simulation and experimental investigations, J. Sound Vib. 492 (2021) 115815, http://dx.doi.org/10.1016/j.jsv.2020.115815.
[24] V. Manchi, C. Sujatha, Torsional vibration reduction of rotating shafts for multiple orders using centrifugal double pendulum vibration absorber, Appl. Acoust. 174 (2021) 107768, http://dx.doi.org/10.1016/j.apacoust.2020.107768.
[25] K. Kadoi, T. Inoue, J. Kawano, M. Kondo, Nonlinear analysis of a torsional vibration of a multidegrees-of-freedom system with centrifugal pendulum vibration absorbers and its suppression, J. Vib. Acoust. 140 (6) (2018) 061008, http://dx.doi.org/10.1115/1.4040042.

[26] B. Geist, V. Ramakrishnan, P. Attibele, W. Resh, Precision requirements for the bifilar hinge slots of a centrifugal pendulum vibration absorber, Precis. Eng. 52 (2018) 1–14, http://dx.doi.org/10.1016/j.precisioneng.2017.08.001.
[27] T.M. Nester, P.M. Schmitz, A.G. Haddow, S.W. Shaw, Experimental observations of centrifugal pendulum vibration absorbers, in: International Symposium on Transport Phenomena and Dynamics of Rotating Machinery, Honolulu (Hawaii), 2004.
[28] S.W. Shaw, P.M. Schmitz, A.G. Haddow, Tautochronic vibration absorbers for rotating systems, J. Comput. Nonlinear Dyn. 1 (4) (2006) 283–293, http://dx.doi.org/10.1115/1.2338652.
[29] C.-P. Chao, S.W. Shaw, The dynamic response of multiple pairs of subharmonic torsional vibration absorbers, J. Sound Vib. 231 (2) (2000) 411–431, http://dx.doi.org/10.1006/jsvi.1999.2722.
[30] L. Shen, B.W. Suter, Bounds for eigenvalues of arrowhead matrices and their applications to hub matrices and wireless communications, EURASIP J. Adv. Signal Process. 2009 (1) (2009) 379402, http://dx.doi.org/10.1155/2009/379402.
[31] C.-P. Chao, S.W. Shaw, The effects of imperfections on the performance of the subharmonic vibration absorber system, J. Sound Vib. 215 (5) (1998) 1065–1099, http://dx.doi.org/10.1006/jsvi.1998.1634.
[32] O. Thomas, C. Touzé, A. Chaigne, Asymmetric non-linear forced vibrations of free-edge circular plates. part II: Experiments, J. Sound Vib. 265 (5) (2003) 1075–1101, http://dx.doi.org/10.1016/S0022-460X(02)01564-X.
[33] A. Givois, J.-J. Tan, C. Touzé, O. Thomas, Backbone curves of coupled cubic oscillators in one-to-one internal resonance: Bifurcation scenario, measurements and parameter identification, Meccanica 55 (3) (2020) 481–503, http://dx.doi.org/10.1007/s11012-020-01132-2.
[34] A. Grolet, Z. Shami, S. Arabi, O. Thomas, Experimental nonlinear localisation in a system of two coupled beams, in: Dynamical System Theory and Applications, Lodz (Poland), 2019, p. 13.
[35] A.H. Nayfeh, Perturbation Methods, in: Wiley Classics Library, Wiley-VCH, Weinheim, 1973, http://dx.doi.org/10.1002/9783527617609.
[36] M. Golubitsky, I. Stewart, D.G. Schaeffer, in: J.E. Marsden, L. Sirovich (Eds.), Singularities and Groups in Bifurcation Theory, in: Applied Mathematical Sciences, Vol. 2, Springer New York, New York, NY, 1988, http://dx.doi.org/10.1007/978-1-4612-4574-2.
[37] A.H. Nayfeh, D.T. Mook, Nonlinear Oscillations, in: Wiley Classics Library, Wiley-VCH, 1995, http://dx.doi.org/10.1002/9783527617586.
[38] L. Guillot, A. Lazarus, O. Thomas, C. Vergez, B. Cochelin, A purely frequency based Floquet-Hill formulation for the efficient stability computation of periodic solutions of ordinary differential systems, J. Comput. Phys. 416 (2020) 109477, http://dx.doi.org/10.1016/j.jcp.2020.109477.
[39] A. Renault, O. Thomas, H. Mahé, Numerical antiresonance continuation of structural systems, Mech. Syst. Signal Process. 116 (2019) 963–984, http://dx.doi.org/10.1016/j.ymssp.2018.07.005.
[40] C.-T. Lee, S.W. Shaw, On the counteraction of periodic torques for rotating systems using centrifugally driven vibration absorbers, J. Sound Vib. 191 (5) (1996) 695–719, http://dx.doi.org/10.1006/jsvi.1996.0151.